Research Article

Investigating the Impact of Soil Models on GPR in Wind Turbine Grounding Systems Across Various Geographical Regions

Omid Heydari; Hassan Moradi; Shahram Karimi; Hamdi Abdi

P A P E R I N F O

Paper history:
Received ?? ??????? 2020
Accepted in revised form ?? ????? 2020

Keywords:
GPR
Grounding System
Wind turbine
Soil modeling
Lightning
CDEGS software
Geographical areas

A B S T R A C T

Grounding systems in wind turbines are critical for lightning protection and managing GPR. This study investigates the influence of different soil models (uniform, two-layer, and three-layer) on GPR across six distinct geographical regions: desert, forest, agricultural, mountainous, coastal, and frozen. Simulations were performed using the CDEGS software on a standard grounding system comprising a ring electrode, horizontal electrodes, and vertical electrodes. The results reveal a strong dependence of GPR on soil characteristics and regional conditions. In desert regions, the high resistivity of dry soil significantly increases GPR, whereas in coastal areas, water-saturated layers markedly reduce GPR. In frozen regions, surface layer freezing substantially elevates GPR despite lower resistivity in deeper layers. The study demonstrates that increasing the complexity of the soil model (i.e., the number of layers) does not necessarily mitigate GPR, underscoring the need for region-specific data in grounding system design. Numerical results show the largest peak GPR for the uniform model in the frozen region during winter (≈2,197,587 V), reduced to 802,833.2 V with the three-layer model (≈63.5% reduction). Overall, in high-resistivity regions (desert, mountainous, frozen) multilayer models yield substantial GPR reductions, whereas in coastal areas changes in soil model cause only minor decreases (≈13.5%). These findings highlight the importance of tailoring grounding system designs to geographical conditions, potentially enhancing the safety and efficiency of wind turbines against lightning strikes.

https://doi.org/...

1. INTRODUCTION

Wind turbines, as a major source of large-scale renewable energy, are installed across a wide range of geographic environments from deserts and mountainous regions to coastal, agricultural and frozen areas. Lightning strikes can induce substantial GPR(Ground Potential Rise), contact voltages, and step voltages, adversely affecting sensitive electrical equipment and personnel safety. Therefore, mitigation of GPR and optimization of the earthing network are critical practical issues for wind farm reliability.

Numerous studies have shown that soil resistivity and its layered profile strongly influence transient earth impedance and peak GPR; assuming homogeneous soil can lead to inaccurate estimates and suboptimal designs [1, 2]. Accurate characterization of soil and attention to layered profiles are therefore essential for reliable prediction of surface potentials and voltages [1, 3].

Several studies have shown that soil electrical properties and their possible frequency dependence can influence transient responses and peak GPR values [1, 3].

Djaborebbi et al. employed transient approaches such as TLM and highlighted the importance of accurate simulation methods for representing transient current distribution and potentials [4].

Visacro et al. pointed out that certain soil electrical characteristics can affect transient analyses; these findings suggest that accounting for soil properties is useful when comparing regions with different resistivities [5].

Field measurements and numerical analyses indicate that multilayer soil models (two- or three-layer horizontal profiles) significantly improve the prediction of overall earth resistance and contact/step voltages compared to uniform models—particularly when surface and sub-surface layers differ in resistivity. Common practice combines Wenner resistivity measurements and inversion/optimization methods (e.g., Sunde formula + genetic algorithms) to extract realistic layered profiles for simulation [3, 6].

Transient GPR analysis commonly employs industry-grade packages such as CDEGS/SES, combined with numerical solvers (FEM/PEEC — COMSOL, XGSLab) and ATP/EMTP or PSCAD for system transient interaction. The combination of field data and accurate numerical modeling is the accepted approach for robust earthing design [7, 8].

Recent research on energy management and smart distribution networks — including Virtual Power Plants (VPPs), Electric Springs (ES), and demand response programs — has demonstrated that coordinated resource-and-load management can substantially improve network performance indices (voltage profile, losses, flexibility and reliability). Although these works do not directly

*Corresponding Author's Email: xxxxxxxxxxxxxxxxxxx

address earthing design, their system-level approach supports the use of realistic soil models and regional analysis for infrastructure and protection decisions [9-11].

Wang et al. have shown that techno-economic co-design of local storage systems (including hydrogen storage) and smart EV charging can substantially affect off-grid planning outcomes; these results underline the importance of incorporating local site characteristics (including soil properties) into engineering analyses when assessing equipment safety and operational performance [12].

Oboudi et al. demonstrate that reliability-constrained transmission expansion planning with simultaneous load and renewable forecasting can improve operational and reliability indices; these findings emphasize the need to couple system-level planning studies with accurate local site modeling (e.g., GPR estimation using realistic soil profiles)[13].

Zadehbagheri et al., focusing on resiliency under extreme weather events, show that optimal placement and sizing of Virtual Power Plants can enhance network resilience; such resiliency-driven planning suggests that higher-level strategies should also account for site-level protections and designs (including grounding and GPR considerations at critical sites)[14].

Naghibi et al., demonstrate that optimal sizing and siting of integrated renewable energy systems (including hydrogen technologies) can significantly improve distribution network technical indices; these outcomes reinforce the need to consider the interaction between system-level planning and local physical parameters (such as soil conditions and resulting GPR effects) [15].

Table 1, summarizes the most relevant studies in the field of wind turbine grounding systems and similar infrastructures, comparing them in terms of study type, soil modeling approach, simulation tools, and geographical coverage. The comparison highlights that the present study adopts a systematic, multi-regional evaluation of soil models (uniform, two-layer, and three-layer), which has been rarely addressed comprehensively in previous works.

Table 1. Comparison of previous works with the present study based on application domain, soil modeling approach, and analysis scope

No.	Reference	Year	Main focus / method	Scope / example geographic coverage	Main limitation	How current work differs / advantage
1	[1] Alipio et al.	2020	Transient response and low-frequency performance analysis of wind farm earthing	Case studies on wind farms	Often limited to single or few turbines; focus on waveforms and frequency dependence	We perform a systematic 1L/2L/3L comparison across **six geographic regions** with fixed electrode geometry and waveform to isolate soil effect.
2	[6]Alipio et al.	2021	GPR due to direct lightning; emphasis on frequency-dependent parameters	Wind farm cases	Emphasis on frequency dependence and waveform analysis; limited regional comparison	Our study focuses on soil profile impacts across regions, complementing waveform-focused analyses.
3	[5] Alipio et al.	2019	Effect of frequency-dependent soil parameters on lightning response	General	Focus on frequency-dependent modeling (high complexity)	We compare 1L/2L/3L models while controlling other variables to highlight layering effects.
4	[4]Djaborebbi et al.	2021	Transient modeling (TLM) of earthing system response	Numerical studies	Focus on numerical method; limited multi-region coverage	Present work uses CDEGS with regional profiles and a multi-region comparison.
5	[3]Sabiha & Elkalashy	2018	Field Wenner measurements + Sunde inversion + genetic algorithm for profile extraction	Field case study	Site-specific study; no broad geographic comparison	We adopt similar profile extraction methods but apply them to **six regions** and run CDEGS simulations for each.
6	[7]CDEGS documentation	2023	Industrial-grade modeling of layered soils and earthing systems	Global / industrial	Powerful tool but requires field data for validation	We use CDEGS as our main simulation platform and feed it with regional soil profiles to enhance result validity.
7	[9]Yao et al.	2023	Energy management: VPP & Electric Springs in SDN	Distribution network (IEEE-69 example)	Focus on energy management/operational metrics rather than earthing design	These references demonstrate system-level methods; we cite them to justify the need for realistic soil models and system-aware analysis.
8	[12]Wang et al.	2025	Stochastic sizing/optimization for hydrogen-based systems (future directions)	Example planning studies in literature	Focus on planning/optimization; different domain but related methodology	We cite these works in limitations/future work to motivate resilience and H2-integration extensions.
9	[14], [15]	2024–2025	VPPs, resilience and integrated-energy planning	Distribution / active DN	Emphasis on resilience/planning	These provide pathways for future expansions discussed in "Dedicated Limitations".

Despite substantial existing work, important gaps remain: (i) a lack of systematic, comparative studies of single-, two- and three-layer soil models across multiple geographic regions; and (ii) limited guidance for engineers on where multilayer modeling is practically necessary. The present study addresses these gaps by providing a systematic comparison across six distinct geographic types [1, 6].

The objective of this study is to systematically investigate the effect of three soil models (1L/2L/3L) on GPR in six geographical regions.

Its innovation can be the systematic comparison of 1L/2L/3L in six regions and pure focus on soil effect while keeping electrode geometry and lightning surge as fixed parameters.

Simulations were also performed using CDEGS software modules and considering fixed geometric parameters (R=15 m ring, 1 m burial, four horizontal 20 m, and four vertical 10 m).

Figure 1 illustrates the overall framework of the present study in graphical abstract form, comprising six geographic regions (desert, forest, agricultural, mountainous, coastal, and frozen), three soil models (uniform, two-layer, and three-layer), and simulations performed using the CDEGS software with fixed electrode geometry and a constant lightning waveform. Outputs include the comparison of GPR across all scenarios to assess the influence of soil modeling under different regional conditions.

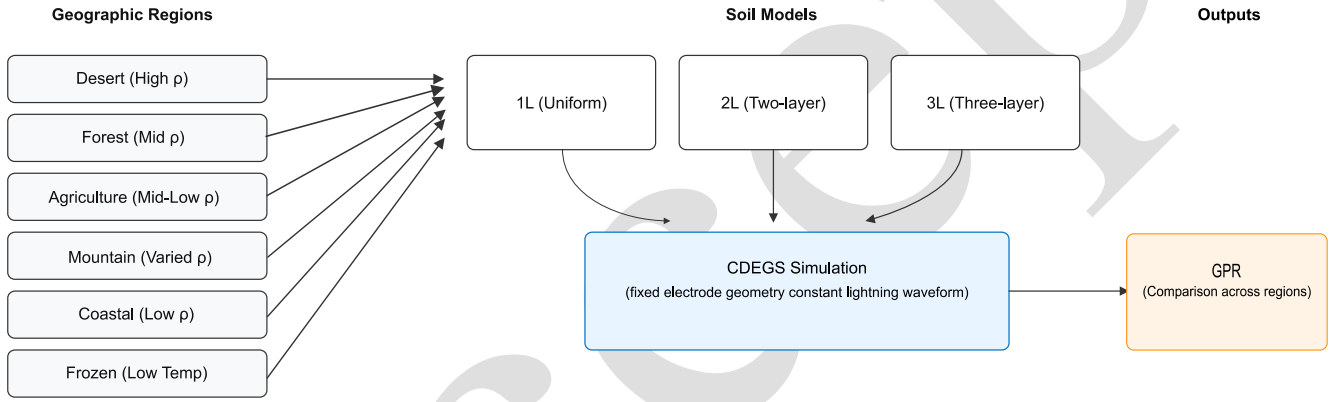

Figure 1. Graphical abstract of the present study

The organization of the paper is as follows: after the current section or the introduction of the paper as the first section, the following sections are discussed in detail as follows: Section 2) Numerical Modeling and Simulation Framework, Section 3) Research Methodology, Section 4: Results and Discussion, Section 5) Dedicated Limitations, Section 6) Conclusion.

In Section 2, the computational theory of this study and the software used are reviewed, and in Section 3, the simulation method and requirements, study cases and scenarios are specified, and in Section 4, the simulation results and outputs are discussed. In Section 5 (Dedicated Limitations), the limitations considered and the assumptions used in this study are also discussed, and it will also be explicitly mentioned that system resilience analyses, integration of hydrogen energy systems, and the investigation of extreme climate events are suitable future options. Finally, in Section 6, the conclusions related to this study are drawn.

2. Numerical Modeling and Simulation Framework

2.1. Maxwell's Equations and Numerical Solution Methods

To determine electromagnetic fields at any point in space, Maxwell's equations must be solved throughout that domain. Solving Maxwell's equations enables precise modeling of grounding system behavior under lightning strikes. These fundamental equations consist of four integral forms: 1) Gauss's law for electric fields, 2) Gauss's law for magnetic fields, 3) Faraday's law, and 4) Ampere-Maxwell law. Typically expressed as partial differential equations (Equations 1.1 to 1.4), they are solved analytically in simple cases. However, when addressed computationally, numerical methods for solving differential equations become indispensable.

$$\nabla . \mathbf{D} = \rho_v \qquad (1.1)$$

$$\nabla \times \mathbf{E} = -\frac{\partial \mathbf{B}}{\partial t} \qquad (1.3)$$

$$\nabla . \mathbf{B} = 0 \qquad (1.2) \qquad \nabla \times \mathbf{H} = -\frac{\partial \mathbf{D}}{\partial t} + \mathbf{J} \qquad (1.4)$$

Various numerical methods exist for solving integral or differential equations, each tailored to specific applications. For time- and frequency-domain problems, two- or three-dimensional scenarios, and differential or integral formulations, techniques such as FEM(Finite Element Method), FDTD(Finite-Difference Time-Domain), MoM(Method of Moments), and FIT(Finite Integration Technique) have been developed and refined to yield optimal solutions. Simulation software addressing such equations typically employs one or more of these methods or combinations thereof[16, 17].

2.2. Method of Moments (MoM)

The MoM is a robust numerical technique for solving integral equations derived from Maxwell's equations, widely applied in electromagnetic field analysis, particularly for computing current distributions in conductive structures. It is especially effective for analyzing high-frequency phenomena, such as electromagnetic interference and lightning effects in complex systems like grounding grids.

Maxwell's equations govern the behavior of electromagnetic fields in a medium. In steady-state or quasi-steady-state problems within conductive media, the electric scalar potential $\emptyset(\mathrm{r})$ at point r due to current density $J(r')$ is computed via the integral equation (2):

$$\emptyset(\mathrm{r}) = \int_V G(r,r').J(r')dV' \qquad (2)$$

where $G(r,r')$ is the Green's function, which models the medium's characteristics, such as soil resistivity ρ. For a homogeneous medium with electrical conductivity $\sigma = \frac{1}{\rho}$, the Green's function is defined as (3):

$$G(r,r') = \frac{1}{4\pi\sigma|r-r'|} \qquad (3)$$

In multilayered media, such as soils with multiple layers, the Green's function incorporates reflection terms to account for boundaries between layers with differing electrical properties (4) :

$$G(r,r') = \frac{1}{4\pi\sigma_1|r-r'|} + \sum_{k=1}^{\infty} R_k \cdot \frac{1}{4\pi\sigma_k|r-r_k'|} \qquad (4)$$

where σ_k is the conductivity of the k-th layer, and R_k are the reflection coefficients.

To implement the Method of Moments, conductive structures (e.g., grounding grids) are discretized into N small segments, each assumed to carry a constant current I_n . The potential at an observation point r_m is then calculated as(5):

$$\emptyset(r_m) = \sum_{n=1}^{N} I_n \int_{S_n} G(r_m,r')dS' \qquad (5)$$

Where S_n represents the area or length of the n-th segment. By enforcing boundary conditions, such as constant potential on conductor surfaces or current continuity, a system of linear equations is established(6):

$$\mathrm{Z} \cdot \mathrm{I} = \mathrm{V} \qquad (6)$$

where Z is the impedance matrix with elements:

$$Z_{mn} = \int_{S_m} \int_{S_n} G(\mathbf{r}_m, \mathbf{r}_n')\, dS_n'\, dS_m, \qquad (7)$$

V is the vector of applied potentials or boundary conditions, and **I** is the vector of unknown currents $\{I_1, I_2, \ldots, I_N\}$.

For high-frequency applications, the impedance matrix includes inductive and capacitive effects(8):

$$Z_{mn} = R_{mn} + j\omega L_{mn} + \frac{1}{j\omega C_{mn}} \qquad (8)$$

where R_{mn}, L_{mn}, and C_{mn} denote the resistance, inductance, and capacitance between segments (m) and (n), respectively. These parameters are derived from Maxwell's equations, incorporating magnetic and electric field interactions(9.1&9.2):

$$L_{mn} = \frac{\mu}{4\pi} \int_{S_m} \int_{S_n} \frac{1}{| \mathbf{r}_m - \mathbf{r}'_n |} \, dS'_n \, dS_m \tag{9.1}$$

$$C_{mn} = \epsilon \int_{S_m} \int_{S_n} \frac{1}{| \mathbf{r}_m - \mathbf{r}'_n |} \, dS'_n \, dS_m, \tag{9.2}$$

where μ is the magnetic permeability and ϵ is the permittivity of the medium.

The system of equations (6) is solved using numerical techniques, such as direct methods (e.g., Gaussian elimination) or iterative methods (e.g., conjugate gradient). This solution yields the current distribution, facilitating the calculation of electromagnetic fields, potentials, and derived quantities like GPR or touch voltages.

The Method of Moments is especially adept at modeling intricate conductor geometries and analyzing high-frequency effects where inductive and capacitive interactions are pronounced, thereby playing a pivotal role in grounding system analysis[18].

2.3 CDEGS

CDEGS(Current Distribution, Electromagnetic Fields, Grounding, and Soil Structure Analysis) is a comprehensive software suite designed for precise analysis of electromagnetic phenomena, including grounding system behavior under high-frequency transients such as lightning, switching, and electromagnetic pulses. As a numerical electromagnetic analysis NEA(Numerical Electromagnetic Analysis) tool, CDEGS solves Maxwell's equations in their full-wave form, leveraging the (MoM). It accounts for all electromagnetic coupling modes, including conduction (via metallic elements, coatings, and soil), magnetic induction, and capacitive effects[7].

CDEGS includes modules such as RESAP, MALT, TRALIN, HIFREQ, FCDIST, MALZ, SPLITS, and FFTSES, which compute conductor currents and electromagnetic fields in arbitrary networks above or below ground under normal, fault, lightning, or transient conditions. It also models simple and multi-component conductors and buried cable systems in complex soil structures. In this study, grounding system simulations were conducted using CDEGS, with outputs post-processed via Python code[19].

2.4. Connection of CDEGS with Maxwell's Equations and MoM

Maxwell's equations in the frequency domain ($\nabla \times E = -j\omega B$) form the basis of calculations in HIFREQ, as MoM converts these equations into integral form for each frequency.

The Green's functions (G(r, r')), which model reflections in multi-layered soils, are derived from solving the Helmholtz equation $(\nabla^2 + k^2)G = -\delta$, which is derived from Maxwell's equations[20].

FFTSES, by transforming between time and frequency domains, enables the use of MoM in HIFREQ for analyzing lightning transients, which would be highly complex without this transformation, as directly solving Maxwell's equations in the time domain is challenging.

2.5. Ground Potential Rise

GPR occurs when substantial electrical current enters the ground. During lightning strikes or short circuits in high-voltage transmission lines, the voltage at the grounded point increases based on current magnitude and grounding system resistance, termed GPR. IEEE Std 80 recommends criteria such as grounding resistance (typically below 10 ohms) and touch/step potentials, often assuming uniform soil. In this study, GPR serves as the primary performance metric for grounding systems, as analyzing its waveform in both time and frequency domains offers comprehensive insights into system behavior under lightning conditions[21].

3. Methodology

In this research, simulations were conducted using the CDEGS software. This software was selected for its robust capabilities in modeling grounding systems, analyzing lightning effects, and supporting multilayered soil models. Within the software, the precise geometry of the grounding system, boundary conditions such as soil layer depths, and lightning-related input parameters were meticulously defined.

For this study, the lightning wave was modeled using the FFTSES module, while soil and grounding system configurations were established using the HIFREQ module in CDEGS. Following simulation execution, GPR outputs at the lightning injection point were obtained, and peak values were extracted using Python code, facilitating final analysis and comparison across various scenarios.

3.1 Lightning Wave Modeling

A typical lightning current waveform is considered, which strikes various ring and mesh grounding systems of wind turbines in two-layer soils with different resistivities. The resulting voltage rises, specifically the GPR, are calculated and analyzed to identify suitable ring and mesh configurations in various scenarios. For simulating the lightning current with parameters (10.1 to 10.3) and coefficients of the modeling function (11.1 to 11.3), a double-exponential time function is used, as shown in equation (12), where the unit of current $I(t)$ is in amperes[22] :

$$\alpha = \frac{0.69}{T_2} \qquad (11.1)$$

$$T_1 = \text{ rise time} \qquad (10.1)$$

$$\beta = \frac{2.2}{T_1} \qquad (11.2)$$

$$T_2 = \text{ pulse duration} \qquad (10.2)$$

$$I_0 = \frac{I_p}{1 + ((\frac{\alpha}{\beta})(\ln\frac{\alpha}{\beta} - 1))} \qquad (11.3)$$

$$I_p = \text{ peak amplitude} \qquad (10.3)$$

$$I(t) = I_0(e^{-\alpha t} - e^{-\beta t}) \qquad (12)$$

For the scenarios under consideration, parameters of a typical lightning strike were set as ($T_1 = 3.4$ μs , $T_2 = 13.5$ μs, and $I_p = 28.51553$ kA)[22]. Using Equations (10) and (11), the parameters for Equation (12) were computed as ($\alpha = 5111.11$ s^{-1} and $\beta = 594594.6$ s^{-1} and $I_0 = 30$ kA). The lightning waveform parameters and the double-exponential coefficients are listed in Table 2; step-by-step calculations for α, β and I₀ are provided in Appendix A.

Table 2 . Lightning waveform parameters and computed double-exponential coefficients (used in simulations)

Parameter	Symbol	Value
Rise time	T_1	3.4 μs
Pulse duration	T_2	13.5 μs
Peak amplitude	I_p	28.51553 kA
Double-exponential α	α	5,111.11 s^{-1}
Double-exponential β	β	594,594.6 s^{-1}
I_0 (model constant)	I_0	30 kA

3.2 Grounding System Configuration Modeling

The grounding system comprises three electrode types: the lightning connection electrode, the electrode linking the geometric center to the main grounding electrodes, and the main grounding electrodes themselves. The lightning connection electrode, a vertical conductor, extends from 0.1 meters above ground to 1 meter below ground at the configuration's geometric center. The connecting electrode links this center to the main grounding electrodes, which form the wind turbine's grounding system. To investigate the impact of soil models on GPR, a standard grounding system was employed, consisting of a ring electrode with a 15-meter radius buried at a 1-meter depth, four 20-meter horizontal electrodes, and four 10-meter vertical electrodes penetrating to an 11-meter depth to assess deeper soil layer effects. Designed per IEEE Std 80, this configuration aims to minimize grounding resistance and optimize GPR. All components of the grounding system used in simulations — including the ring electrode, the horizontal and vertical electrodes, the lightning connection rod, and the connecting conductor — are modeled as bare copper conductors with a cross-sectional radius of 0.0067056 m (no coating or insulation). This makes the conductor material and geometry consistent across all simulation elements

Figure 2 Configuration of the extended ring grounding system with additional horizontal and vertical electrodes.

Table 3. shows the identical grounding configuration applied across all simulations.

Table 3 . Grounding geometry used in all scenarios

Parameter	Value
Ring radius (R)	15 m
Ring burial depth	1 m
Number / length of horizontal electrodes	4 × 20 m
Number / length of vertical electrodes	4 × 10 m (depth penetration to 11 m considered in some cases)
Lightning injection point	Geometric center (0.1 m above ground) connected via a vertical rod to 1 m below ground
Electrode material	Bare copper (all electrodes including lightning connection rod)
Electrode cross-section radius	0.0067056 m

It should be noted that the same grounding configuration (R = 15 m ring + 4×20 m horizontal + 4×10 m vertical) was used for all regions and scenarios (see Table 3). This methodological choice isolates the pure effect of soil-model variation (1L/2L/3L) on GPR by keeping electrode geometry and lightning waveform constant. The chosen configuration corresponds to commonly used earthing arrangements for wind turbine foundations and aligns with practical industry guidance (e.g., IEC recommendations on wind turbine lightning protection).

3.3 Soil Modeling

Three soil models were utilized. First, the uniform model assumes a homogeneous soil layer with constant electrical parameters. Second, the two-layer horizontal model divides soil into two layers, each with distinct thickness and electrical properties. Third, the three-layer horizontal model stratifies soil into three layers with varying thicknesses, with electrical properties based on real regional characteristics.

Figure 3 Side view of the three-layer soil model, where $\boldsymbol{l_1}$ ،$\boldsymbol{l_2}$ and $\boldsymbol{l_3}$ denote the thicknesses of the top, middle, and bottom layers, respectively, and $\boldsymbol{l_{Burial}}$ is the burial depth of the ring and horizontal electrodes. Additionally, $\boldsymbol{\rho_1}$ and $\boldsymbol{\epsilon_{r_1}}$ are the resistivity and relative permittivity of the top layer, $\boldsymbol{\rho_2}$ and $\boldsymbol{\epsilon_{r_2}}$ for the middle layer, and $\boldsymbol{\rho_3}$ and $\boldsymbol{\epsilon_{r_3}}$ for the bottom layer.

To accurately model soil electrical behavior in CDEGS simulations, electrical parameters—resistivity, relative permittivity, and layer thicknesses—were determined for six geographical regions (desert, forest, agricultural, mountainous, cold, and coastal) and seasons (summer and winter, except coastal areas with uniform seasonal conditions). These representative values, based on typical soil properties, environmental conditions (humidity, temperature, composition), and scientific/industrial standards, effectively simulate real-world soil behavior[23].

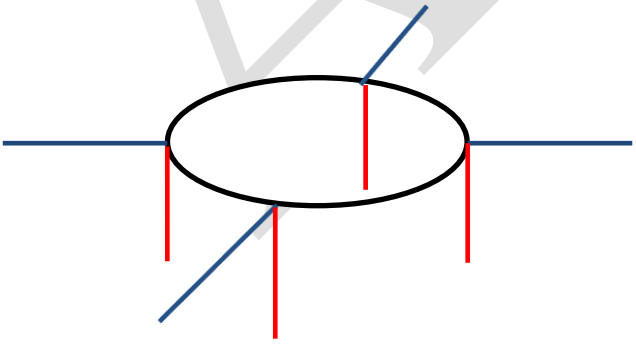

Figure 2. Extended loop grounding system configuration with additional horizontal and vertical electrodes

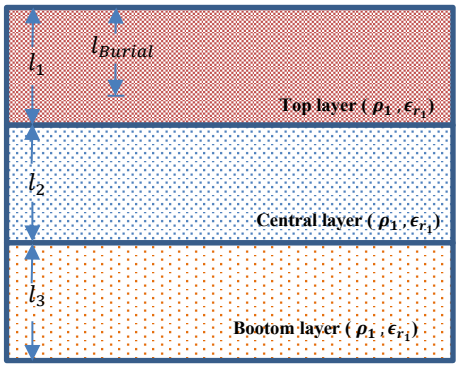

Figure 3. Three-layer soil model (side view)

3.3.1 General Explanation of Parameters

- Relative Permeability: Set to 1 for all models, as the soils lack significant magnetic properties, consistent with electrical geology studies.
- Resistivity: Dependent on humidity, temperature, mineral composition, and structure, ranging from thousands of ohm-meters in dry soils to tens in moist or saline soils.
- Relative Permittivity: Influenced by moisture and composition, with higher values in wet soils (due to water's permittivity of ~80) and lower values (2-5) in dry soils.
- Layer Thickness: Determined by geological heterogeneity and moisture/frost penetration, with surface layers typically thinner (e.g., 3 meters for the first layer, 4 meters for the second, and infinite for the third), aligning with common multilayer models.

3.3.2 Justification of Values for Each Region

a. Desert Areas

- Summer: High resistivity (4000 ohm-meters, uniform model) reflects extreme dryness, consistent with 1000-5000 ohm-meters for dry soils. Low permittivity (2) indicates minimal moisture. Multilayer models show reduced resistivity in deeper layers (2000, 1000 ohm-meters), suggesting conductive layers or slight moisture.
- Winter: Resistivity drops to 3600 ohm-meters due to potential rainfall, though soil remains dry.

b. Forest Areas

- Summer: Moderate resistivity (300 ohm-meters) reflects moisture and organic content, aligning with 100-500 ohm-meters for forest soils. High permittivity (20) confirms moisture. Deeper layers (800, 200 ohm-meters) indicate compositional shifts.
- Winter: Resistivity rises to 4000 ohm-meters due to surface freezing, with permittivity (3) reflecting reduced moisture.

c. Agricultural Areas

- Summer: Resistivity (3000 ohm-meters) suggests drier conditions, with permittivity (5) indicating moderate moisture. Deeper layers (800, 400 ohm-meters) suggest groundwater.
- Winter: Resistivity drops to 200 ohm-meters due to rainfall/irrigation, with permittivity (25) confirming water presence.

d. Mountainous Areas

- Summer: High resistivity (5000 ohm-meters) reflects rocky, dry soil, consistent with 1000-10000 ohm-meters. Permittivity (4) indicates dryness. Deeper layers (2000, 800 ohm-meters) suggest geological variations.
- Winter: Resistivity increases to 7000 ohm-meters due to freezing, with permittivity (3) aligning with cold conditions.

e. Cold Areas

- Summer: Resistivity (6000 ohm-meters) reflects dryness and low temperatures. Deeper layers (2000, 800 ohm-meters) show reduced resistivity.
- Winter: Resistivity rises to 8000 ohm-meters due to severe freezing, with permittivity (3) indicating low moisture.

f. Coastal Areas

- Summer and Winter: Low resistivity (100 ohm-meters) reflects high moisture and salinity, consistent with 2-100 ohm-meters. Permittivity (25) confirms water presence. Deeper layers (200, 50 ohm-meters) reflect salinity/moisture variations.

In conclusion, soil electrical parameters in Table 4 were selected as representative values based on geological, environmental, and reported data, accurately modeling soil behavior across diverse conditions. For practical applications, collecting region-specific soil data is recommended for enhanced precision.

For all soil models in this study, the relative permeability (p.u.) of the soil is assumed to be 1.

3.4 Assumptions

To simplify the modeling process, several assumptions were adopted. First, the frequency dependence of soil electrical parameters and soil ionization phenomena are excluded. Second, the grounding system is assumed fixed, comprising a ring electrode with horizontal and vertical extensions. Third, the soil model is limited to horizontal layers, excluding more complex configurations such as vertical, spherical, or exponential layers. These assumptions align with common practices in similar studies but do not encompass all real-world conditions. Additionally, all electrodes (mesh, ring, and connecting) are assumed to be copper. Implications are discussed in Section 5.

4. Results and Discussion

In the simulation of the case studies, the lightning wave under investigation is applied over a time range of 0 to 50 microseconds. The injection point of the lightning wave and the observation point for the GPR voltage are located 0.1 meters above the ground surface at the center of the xy-plane. The lightning wave is connected from the injection point to the geometric center of the grounding system via a vertical rod. All electrodes are made of copper with a radius of 0.0067056 meters, and their relative permittivity and relative permeability are assumed to be 1. Additionally, all electrodes used are bare, without any coating or insulation.

This section presents the results of simulations conducted using the CDEGS software to evaluate GPR in wind turbine grounding systems under lightning strikes. For each geographical region, GPR time-domain plots and bar charts of peak GPR values are provided for summer and winter seasons (except for the coastal region, where seasonal conditions are assumed uniform). The analysis focuses on the influence of soil models (uniform, two-layer, and three-layer) on GPR and identifies regional and seasonal patterns.

The grounding-system response to a lightning impulse is a time-domain transient containing rich temporal information (peak, time-to-peak, slope, frequency content). For engineering assessment of GPR, presenting the full time-domain waveform and extracting peak values is the most directly relevant approach. Statistical visualizations (e.g., boxplots) are valuable for summarizing distributions, however for this study — which focuses on isolating soil-model effects under fixed electrode geometry and representative regional profiles — time-domain plots together with peak-comparison bar charts offer clearer engineering interpretation. A comprehensive statistical analysis (means, standard deviations, energy metrics) is being prepared as a follow-up study and will be reported separately (see Section 5: Limitations & Future Work).

Table 4. Thickness and electrical parameters of soil in various geographical regions and seasons for uniform, two-layer, and three-layer models.

Region type	Season type	Soil model	Soil Layer	Thickness (Meter)	Resistivity(Ohm-Meter)	Relative (p.u) Permitivity
Desert Areas	**Summer**	Uniform Soil	Total layer	∞	4000	2
		Two-Layered Soil	Top Layer	3	4000	2
			Bottom Layer	∞	2000	5
		Three-Layered Soil	Top Layer	3	4000	2
			Central Layer	4	2000	5
			Bottom Layer	∞	1000	10
	Winter	Uniform Soil	Total layer	∞	3600	2
		Two-Layered Soil	Top Layer	3	3600	2
			Bottom Layer	∞	1800	5
		Three-Layered Soil	Top Layer	3	3600	2
			Central Layer	4	1800	5
			Bottom Layer	∞	900	10
Forest Areas	**Summer**	Uniform Soil	Total layer	∞	300	20
		Two-Layered Soil	Top Layer	3	300	20
			Bottom Layer	∞	800	15
		Three-Layered Soil	Top Layer	3	300	20
			Central Layer	4	800	15
			Bottom Layer	∞	200	30
	Winter	Uniform Soil	Total layer	∞	4000	3
		Two-Layered Soil	Top Layer	3	4000	3
			Bottom Layer	∞	1000	10
		Three-Layered Soil	Top Layer	3	4000	3
			Central Layer	4	1000	10
			Bottom Layer	∞	500	25
Agricultural Areas	**Summer**	Uniform Soil	Total layer	∞	3000	5
		Two-Layered Soil	Top Layer	3	3000	5
			Bottom Layer	∞	800	15
		Three-Layered Soil	Top Layer	3	3000	5
			Central Layer	4	800	15
			Bottom Layer	∞	400	25
	Winter	Uniform Soil	Total layer	∞	200	25
		Two-Layered Soil	Top Layer	3	200	25
			Bottom Layer	∞	100	40
		Three-Layered Soil	Top Layer	3	200	25
			Central Layer	4	100	40
			Bottom Layer	∞	500	20
Mountain Areas	**Summer**	Uniform Soil	Total layer	∞	5000	4
		Two-Layered Soil	Top Layer	3	5000	4
			Bottom Layer	∞	2000	10
		Three-Layered Soil	Top Layer	3	5000	4
			Central Layer	4	2000	10
			Bottom Layer	∞	800	20
	Winter	Uniform Soil	Total layer	∞	7000	3
		Two-Layered Soil	Top Layer	3	7000	3
			Bottom Layer	∞	3000	6
		Three-Layered Soil	Top Layer	3	7000	3
			Central Layer	4	3000	6
			Bottom Layer	∞	1000	15
Cold Areas	**Summer**	Uniform Soil	Total layer	∞	6000	5
		Two-Layered Soil	Top Layer	3	6000	5
			Bottom Layer	∞	2000	12
		Three-Layered Soil	Top Layer	3	6000	5
			Central Layer	4	2000	12
			Bottom Layer	∞	800	18
	Winter	Uniform Soil	Total layer	∞	8000	3
		Two-Layered Soil	Top Layer	3	8000	3
			Bottom Layer	∞	3000	8
		Three-Layered Soil	Top Layer	3	8000	3
			Central Layer	4	3000	8
			Bottom Layer	∞	1500	12
Coastal Areas	**Summer / Winter**	Uniform Soil	Total layer	∞	100	25
		Two-Layered Soil	Top Layer	3	100	25

	Bottom Layer	∞	200	80
Three-Layered Soil	Top Layer	3	100	25
	Central Layer	4	200	80
	Bottom Layer	∞	50	40

As observed in Figures 4,5,6 and 7, in the desert region—characterized by dry soil and high resistivity—the use of multilayer soil models significantly reduces peak GPR. In summer, the peak GPR for the uniform (single-layer) model is 1,107,882 V, which decreases to 701,091.7 V (a 36.7% reduction) with the two-layer model and further to 504,517.4 V (a 28.1% reduction relative to the two-layer model) with the three-layer model. In winter, the peak GPR decreases from 998,236.5 V in the uniform model to 633,778.6 V in the two-layer model (a 36.5% reduction) and then to 461,419.5 V in the three-layer model (a 27.2% reduction relative to the two-layer model). This trend indicates a consistent reduction in peak GPR with an increasing number of layers in both seasons. This reduction is attributed to the better distribution of lightning current into deeper layers with lower resistivity in multilayer models.

As shown in Figures 8,9,10 and 11, in the forest region, seasonal conditions markedly influence GPR behavior. In summer, the peak GPR for the uniform model is 222,271.8 V, the lowest value observed. This increases to 265,347.7 V (a 19.4% increase) with the two-layer model and decreases to 234,135.3 V (an 11.8% reduction relative to the two-layer model) with the three-layer model. In winter, however, the peak GPR for the uniform model rises sharply to 1,107,012 V, decreasing to 454,773 V (a 58.9% reduction) with the two-layer model and further to 370,819.8 V (an 18.5% reduction relative to the two-layer model) with the three-layer model. These results suggest that the uniform model performs best in summer, while the three-layer model excels in winter. This variation is attributed to changes in soil moisture and its effect on resistivity.

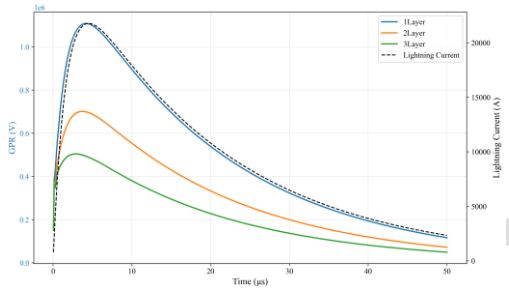

Figure 4. Lightning wave and GPR graphs in desert areas and summer season for horizontal soil models uniform , two-layer and three-layer

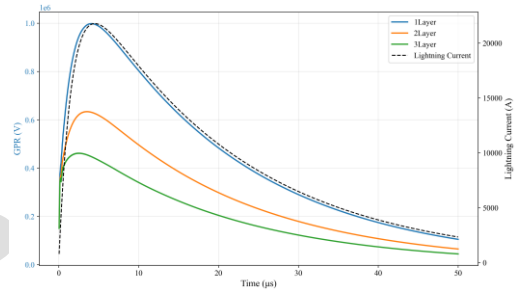

Figure 5. Lightning wave and GPR graphs in desert areas and winter season for horizontal soil models uniform , two-layer and three-layer

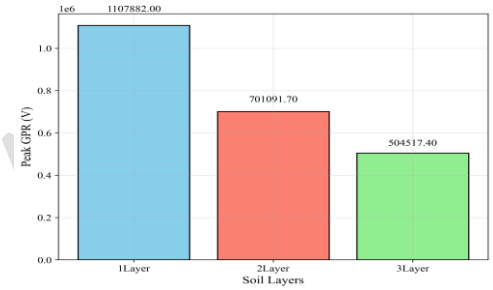

Figure 6. GPR peak bar graph in desert areas and summer season for horizontal soil models uniform , two-layer and three-layer

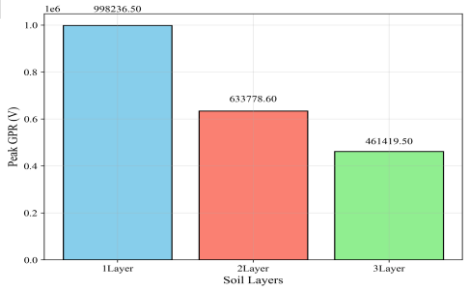

Figure 7. GPR peak bar graph in desert areas and winter season for horizontal soil models uniform , two-layer and three-layer

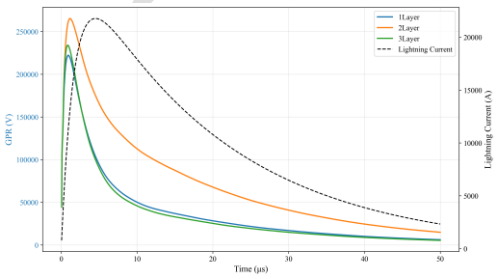

Figure 8. Lightning wave and GPR graphs in forest areas and summer season for horizontal soil models

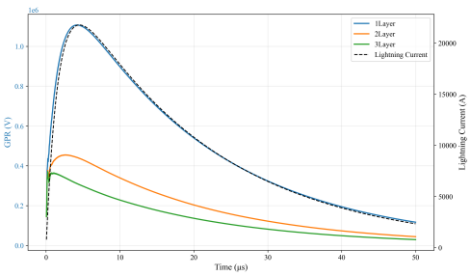

Figure 9. Lightning wave and GPR graphs in forest areas and winter season for horizontal soil models

uniform , two-layer and three-layer

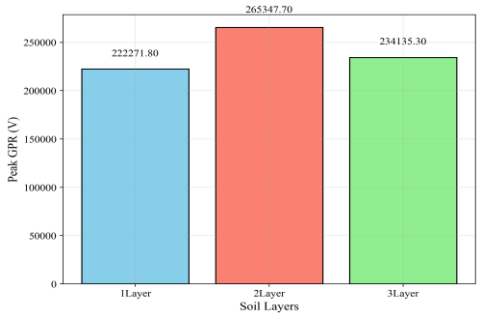

Figure 10. GPR peak bar graph in forest areas and summer season for horizontal soil models uniform , two-layer and three-layer

uniform , two-layer and three-layer

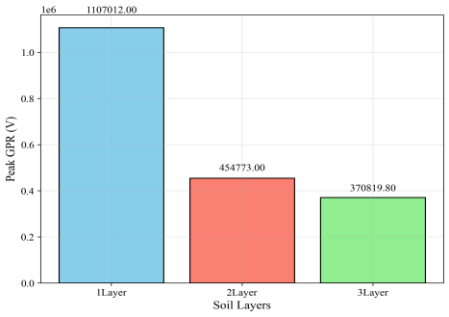

Figure 11. GPR peak bar graph in forest areas and winter season for horizontal soil models uniform , two-layer and three-layer

As depicted in Figures 12,13,14 and 15, in the agricultural region, the peak GPR in summer for the uniform model is 832,480.2 V, decreasing to 379,717.1 V (a 54.4% reduction) with the two-layer model and to 365,533 V (a 3.7% reduction relative to the two-layer model) with the three-layer model. In winter, the peak GPR for the uniform model is 189,255.2 V, reducing to 173,916.2 V (an 8.1% reduction) with the two-layer model and increasing slightly to 182,653.6 V (a 5.0% increase relative to the two-layer model) with the three-layer model. These findings indicate that the three-layer model yields the lowest peak GPR in summer, while the two-layer model performs best in winter. This variable behavior is linked to differences in agricultural soil properties, including moisture and electrical conductivity, across seasons.

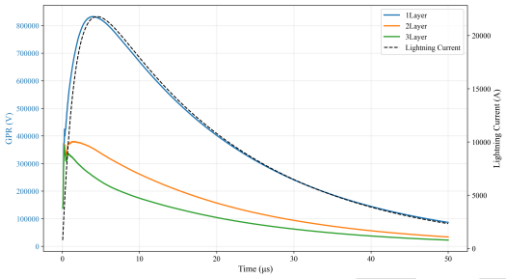

Figure 12. Lightning wave and GPR graphs in agricultural areas and summer season for horizontal soil models uniform , two-layer and three-layer

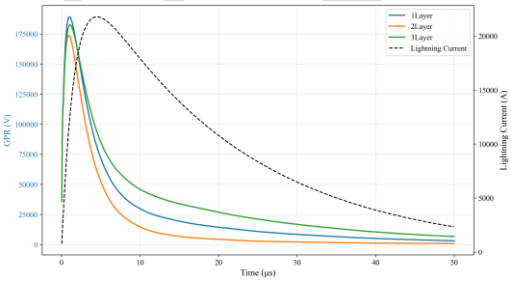

Figure 13. Lightning wave and GPR graphs in agricultural areas and winter season for horizontal soil models uniform , two-layer and three-layer

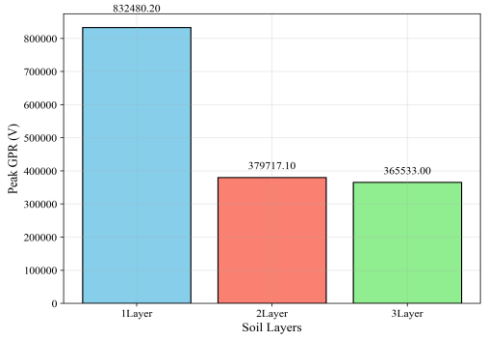

Figure 14. GPR peak bar graph in agricultural areas and summer season for horizontal soil models uniform , two-layer and three-layer

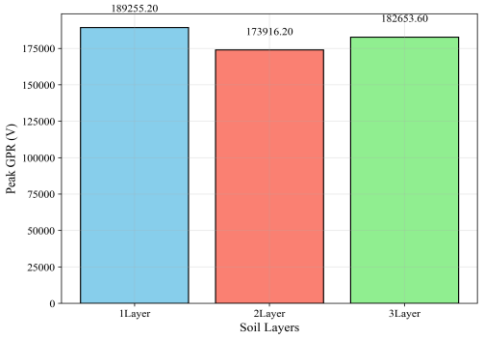

Figure 15. GPR peak bar graph in agricultural areas and winter season for horizontal soil models uniform , two-layer and three-layer

As illustrated in Figures 16,17,18 and 19, in the mountainous region, the peak GPR in summer for the uniform model is 1,376,495 V, decreasing to 750,228.4 V (a 45.5% reduction) with the two-layer model and to 481,227.2 V (a 35.9% reduction relative to the two-layer model) with the three-layer model. In winter, the peak GPR for the uniform model is 1,925,471 V, reducing to 1,093,948 V (a 43.2% reduction) with the two-layer model and to 625,582.2 V (a 42.8% reduction relative to the two-layer model) with the three-layer model. These results demonstrate that increasing the number of layers consistently reduces peak GPR in both seasons, with the three-layer model exhibiting the best performance. This reduction is attributed to the heterogeneity of mountainous soil and the presence of deeper layers with lower resistivity.

As presented in Figures 20,21,22 and 23, in the frozen region, the peak GPR in summer for the uniform model is 1,643,587 V, decreasing to 791,952.5 V (a 51.8% reduction) with the two-layer model and to 504,409.4 V (a 36.3% reduction relative to the two-

layer model) with the three-layer model. In winter, the peak GPR for the uniform model is 2,197,587 V, reducing to 1,139,922 V (a 48.1% reduction) with the two-layer model and to 802,833.2 V (a 29.6% reduction relative to the two-layer model) with the three-layer model. These results highlight the superiority of the three-layer model in both seasons, linked to the high-resistivity frozen surface layer and lower-resistivity deeper layers in multilayer models.

As shown in Figures 24and 25, in the coastal region—where seasonal conditions are assumed uniform—the peak GPR for the uniform model is 137,727.1 V, decreasing to 119,138.5 V (a 13.5% reduction) with the two-layer model and slightly increasing to 119,162.4 V (a negligible 0.02% increase relative to the two-layer model) with the three-layer model. These results indicate that the two-layer model provides the lowest peak GPR, though the difference between the two- and three-layer models is minimal. This behavior is attributed to the water-saturated soil and low resistivity in coastal regions, where changes in soil model have limited impact on GPR.

In other words, in coastal areas, the topsoil is typically low-resistivity (e.g., ≈100 Ω·m) due to moisture and salinity and has high permittivity. Intermediate layers can exhibit relatively higher resistivity due to evaporation-driven processes or sediment layers, while deeper layers may become saturated with saline groundwater and again show much lower resistivity (e.g., the [100 | 200 | 50] Ω·m profile). In such three-layer configurations a deep, very conductive layer enables easier current penetration to depth and reduces the overall effective grounding resistance, which explains why GPR does not necessarily increase and may instead reduce slightly. Numerical checks (mesh/refinement and convergence in CDEGS) were performed and did not indicate modeling instability artifacts; hence the observed behavior is consistent with plausible coastal hydrogeological profiles.

Figure 26 provides a comprehensive overview of peak GPR across all geographical regions, seasons, and soil models. The highest peak GPR is observed in the frozen region in winter with the uniform model (2,197,587 V), while the lowest is in the coastal region with the two-layer model (119,138.5 V). In regions with high soil resistivity (desert, mountainous, and frozen), increasing the number of layers consistently reduces peak GPR, with the three-layer model performing best. For instance, in the frozen region in winter, peak GPR decreases from 2,197,587 V in the uniform model to 802,833.2 V in the three-layer model (a 63.5% reduction), the largest percentage reduction observed. In contrast, in the coastal region, changing the soil model results in only a 13.5% reduction in peak GPR.

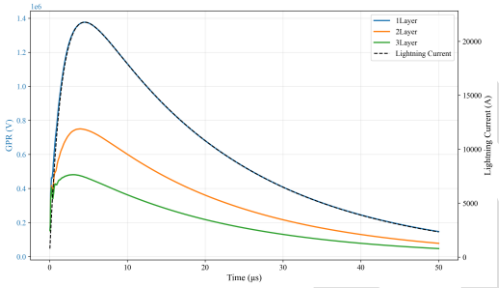

Figure 16. Lightning wave and GPR graphs in mountainous areas and summer season for horizontal soil models uniform , two-layer and three-layer

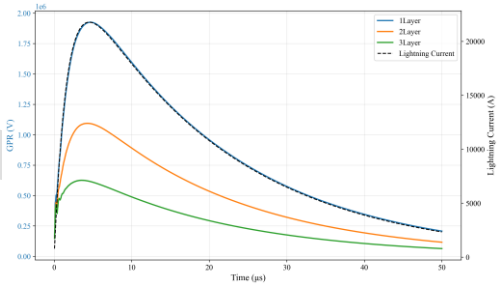

Figure 17. Lightning wave and GPR graphs in mountainous areas and winter season for horizontal soil models uniform , two-layer and three-layer

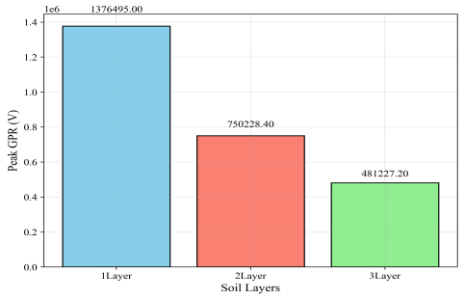

Figure 18. GPR peak bar graph in mountainous areas and summer season for horizontal soil models uniform , two-layer and three-layer

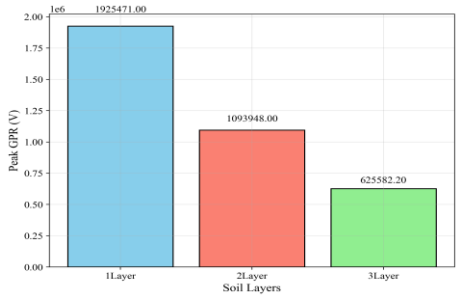

Figure 19. GPR peak bar graph in mountainous areas and winter season for horizontal soil models uniform , two-layer and three-layer

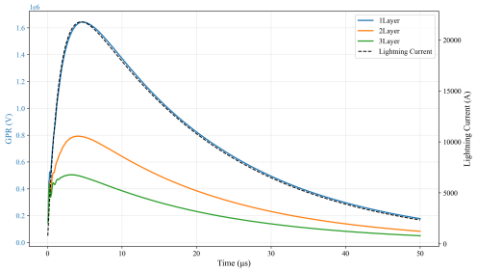

Figure 20. Lightning wave and GPR graphs in frozen areas and summer season for horizontal soil models uniform , two-layer and three-layer

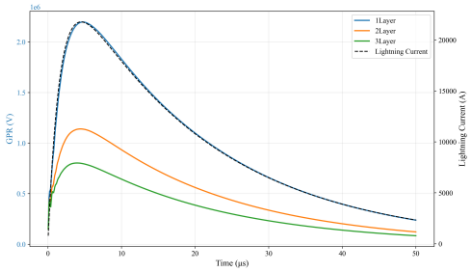

Figure 21. Lightning wave and GPR graphs in frozen areas and winter season for horizontal soil models uniform , two-layer and three-layer

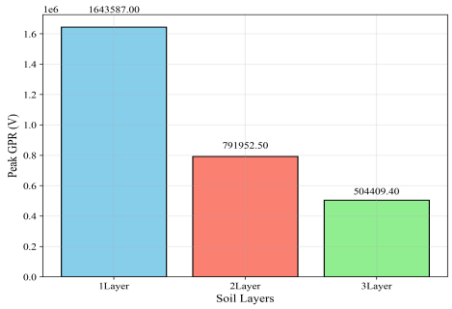

Figure 22. GPR peak bar graph in frozen areas and summer season for horizontal soil models uniform , two-layer and three-layer

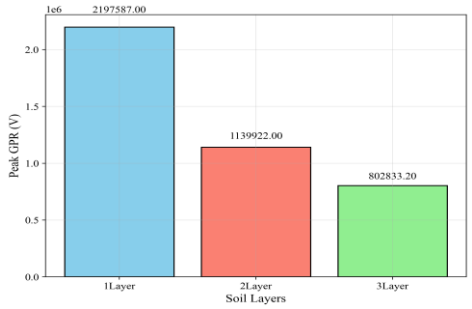

Figure 23. GPR peak bar graph in frozen areas and winter season for horizontal soil models uniform , two-layer and three-layer

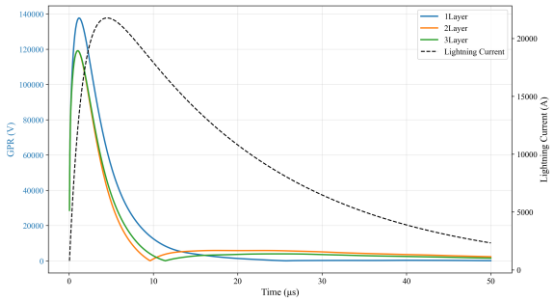

Figure 24. Lightning wave and GPR graphs in coastal areas and summer/winter season for horizontal soil models uniform , two-layer and three-layer

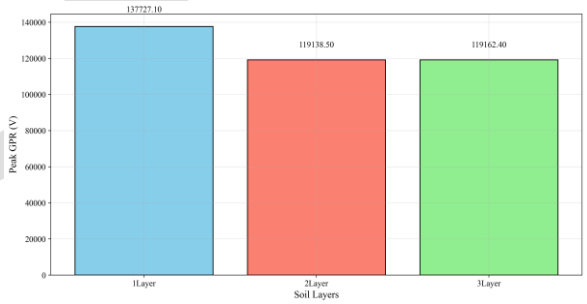

Figure 25. GPR peak bar graph in coastal areas and summer/winter season for horizontal soil models uniform , two-layer and three-layer

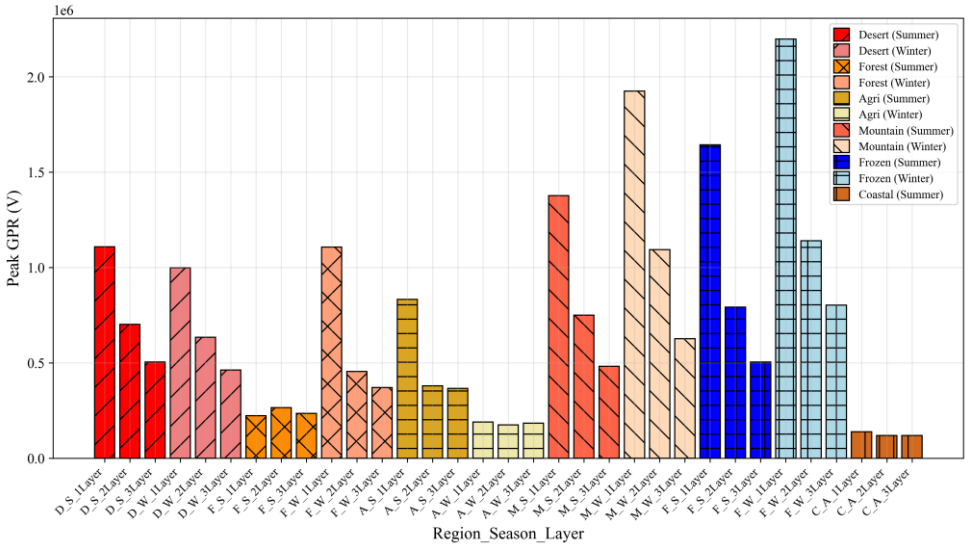

Figure 26. Comparison of peak GPR voltage for all geographical regions, seasons, and soil models

In forest and agricultural regions, patterns vary. In the forest region, the uniform model in summer (222,271.8 V) and the three-layer model in winter (370,819.8 V) yield the lowest peak GPR values. In the agricultural region, the three-layer model in summer (365,533 V) and the two-layer model in winter (173,916.2 V) perform best. These findings suggest that soil model selection should account for regional and seasonal conditions, as increasing the number of layers does not always reduce GPR.

The results of this study emphasize the importance of using real soil data in designing wind turbine grounding systems. In dry and frozen regions, multilayer modeling can significantly enhance safety, whereas in coastal regions, simpler models may suffice. Engineers and designers should select appropriate soil models based on regional and seasonal characteristics to ensure optimal lightning protection.

5. Limitations and Future Work

This section lists the principal methodological limitations that may affect the generality of findings and outlines recommended future research:

a. **Neglect of frequency-dependent soil parameters:** Soil electrical properties were treated as frequency-independent to isolate pure layering effects. Previous works indicate that frequency dependence can affect transient responses, particularly in high-resistivity soils [3, 6]. Frequency-dependent modeling is recommended for targeted follow-up studies.

b. **Exclusion of soil ionization:** Ionization effects near conductors under strong impulses can alter local conductivity and current paths [17]. Modeling ionization requires nonlinear approaches and experimental calibration and was therefore excluded here.

c. **Horizontal-layer assumption only:** Horizontally layered soil models are the most common and practical representation for many field sites and are widely used in earthing studies. Nonetheless, vertical inhomogeneities, channels, or localized anomalies would require 3D or non-horizontal modeling to capture accurately. The rationale is discussed in Section 3.3.

d. **Fixed electrode geometry and lightning waveform:** Geometry and waveform were kept constant across regions to isolate soil-model effects; while appropriate for systematic comparison, practical design should consider geometric variations and interconnection effects.

e. **Parameter uncertainty:** Soil parameters used are representative; full uncertainty/sensitivity analysis is recommended as a follow-up.

f. **Suggested extensions:** Future work should include (i) frequency-dependent and ionization-inclusive modeling, (ii) 3D non-horizontal soil heterogeneity studies, (iii) comprehensive statistical analysis (means, stds, energy metrics), and (iv) field campaigns for validation.

See Assumptions (Section 3.4) for modeling choices.

6. Conclusion

This study used CDEGS simulations to investigate the influence of soil modeling choices (1L/2L/3L) on Ground Potential Rise (GPR) for wind turbine earthing systems across six geographic regions. Key findings are:

- In high-resistivity regions (desert, mountainous, frozen), multilayer soil models yield substantial reductions in peak GPR (example: frozen region, winter — peak reduced from ≈2,197,587 V to ≈802,833.2 V with the 3-layer model, ≈63.5% reduction).
- In conductive regions such as coastal areas, soil-model changes have limited impact on peak GPR (≈13.5% reduction); thus simpler models may suffice for preliminary design in such locales.
- Increased soil-model complexity does not guarantee GPR reduction in all cases; outcomes depend strongly on local layer resistivities, thicknesses and seasonal conditions.

  Practical implication: Engineers should incorporate site-specific soil data and seasonal variability when designing wind turbine earthing; multilayer characterization is particularly important in high-resistivity environments.

Limitations & future work: Frequency-dependent soil properties, soil ionization effects, and vertical/non-horizontal heterogeneity were not included (see Section 5). A comprehensive statistical study (means, standard deviations, energy-based metrics) is underway as a follow-up to strengthen quantitative comparisons.

REFERENCES

[1] R. Alipio, M. T. C. de Barros, M. A. O. Schroeder, and K. Yamamoto, "Analysis of the lightning impulse and low-frequency performance of wind farm grounding systems," *Electric power systems research,* vol. 180, p. 106068, 2020.

[2] Y. Hu *et al.*, "A new grounding resistance reduction method for wind turbines by grounding grid connection in limited areas," *Frontiers in Energy Research,* vol. 10, p. 830628, 2022.
[3] N. A. Sabiha and N. I. Elkalashy, "Evaluation of Grounding System Design for Wind Farm Using COMSOL," *International Journal of Applied Engineering Research,* vol. 13, no. 6, pp. 4124-4132, 2018.
[4] A. Djaborebbi, B. Zegnini, and D. Mahi, "Analysis of the performance of grounding grids buried in heterogeneous soil under impulse current," *Indonesian Journal of Electrical Engineering and Computer Science,* vol. 22, no. 1, pp. 571-579, 2021.
[5] R. Alipio, D. Conceição, A. De Conti, K. Yamamoto, R. N. Dias, and S. Visacro, "A comprehensive analysis of the effect of frequency-dependent soil electrical parameters on the lightning response of wind-turbine grounding systems," *Electric Power Systems Research,* vol. 175, p. 105927, 2019.
[6] R. Alipio, M. Guimarães, L. Passos, D. Conceição, and M. T. C. de Barros, "Ground potential rise in wind farms due to direct lightning," *Electric Power Systems Research,* vol. 194, p. 107110, 2021.
[7] S. E. S. Technologies. "CDEGS: Current Distribution, Electromagnetic Fields, Grounding and Soil Structure Analysis[Computer software]." Safe Engineering Services & Technologies (SES). https://www.sestech.com (accessed 2025-08-09.
[8] E. Software. "Wind Farm Earthing Design and Modelling Guide (technical guide)." Elek. https://elek.com/articles/earthing-design-and-modelling-guide-for-wind-farms (accessed 2025-08-09.
[9] M. Yao, Z. Moradi, S. Pirouzi, M. Marzband, and A. Baziar, "Stochastic economic operation of coupling unit of flexi-renewable virtual power plant and electric spring in the smart distribution network," *IEEE Access,* vol. 11, pp. 75979-75992, 2023.
[10] R. B. Navesi, A. F. Naghibi, H. Zafarani, H. Tahami, and S. Pirouzi, "Reliable operation of reconfigurable smart distribution network with real-time pricing-based demand response," *Electric Power Systems Research,* vol. 241, p. 111341, 2025.
[11] J. Zhang, H. Wu, E. Akbari, L. Bagherzadeh, and S. Pirouzi, "Eco-power management system with operation and voltage security objectives of distribution system operator considering networked virtual power plants with electric vehicles parking lot and price-based demand response," *Computers and Electrical Engineering,* vol. 121, p. 109895, 2025.
[12] R. Wang, E. Akbari, L. Bagherzadeh, and S. Pirouzi, "Stochastic economic sizing of hydrogen storage-based renewable off-grid system with smart charge of electric vehicles according to combined hydrogen and power model," *Journal of Energy Storage,* vol. 108, p. 115171, 2025.
[13] M. H. Oboudi, H. Hamidpour, M. Zadehbagheri, S. Safaee, and S. Pirouzi, "Reliability-constrained transmission expansion planning based on simultaneous forecasting method of loads and renewable generations," *Electrical Engineering,* vol. 107, no. 1, pp. 1141-1161, 2025.
[14] M. Zadehbagheri, M. Dehghan, M. Kiani, and S. Pirouzi, "Resiliency-constrained placement and sizing of virtual power plants in the distribution network considering extreme weather events," *Electrical Engineering,* vol. 107, no. 2, pp. 2089-2105, 2025.
[15] A. F. Naghibi, E. Akbari, S. Shahmoradi, S. Pirouzi, and A. Shahbazi, "Stochastic economic sizing and placement of renewable integrated energy system with combined hydrogen and power technology in the active distribution network," *Scientific Reports,* vol. 14, no. 1, p. 28354, 2024.
[16] R. Guizán, I. Colominas, J. París, I. Couceiro, and F. Navarrina, "Numerical analysis and safety design of grounding systems in underground compact substations," *Electric Power Systems Research,* vol. 203, p. 107627, 2022.
[17] B. Nekhoul, B. Harrat, A. Boutadjine, and M. Melit, "A simplified numerical modeling of the transient behavior of grounding systems considering soil ionization," *Electric Power Systems Research,* vol. 211, p. 108182, 2022.
[18] M. R. Alemi, S. H. H. Sadeghi, and H. Askarian-Abyaneh, "A marching-on-in-time method of moments for computation of transient potential rise of grounding grids exposed to lightning strikes," *IEEE Transactions on Electromagnetic Compatibility,* vol. 65, no. 5, pp. 1484-1491, 2023.
[19] Q. Ma, J. Xie, Z. Lu, L. Liu, X. Cao, and R. Li, "Analysis of grounding impedance spectrum based on CDEGS with different soil characteristics," in *2022 IEEE International Conference on High Voltage Engineering and Applications (ICHVE)*, 2022: IEEE, pp. 1-4.
[20] Y. Dan, Z. Zhang, H. Zhao, Y. Li, H. Ye, and J. Deng, "A novel segmented sampling numerical calculation method for grounding parameters in horizontally multilayered soil," *International Journal of Electrical Power & Energy Systems,* vol. 126, p. 106586, 2021.
[21] A. Taher, A. Said, T. Eliyan, and A. Hafez, "Analysis and mitigation of ground grid lightning potential rise," *Transactions on Electrical and Electronic Materials,* vol. 21, pp. 305-314, 2020.
[22] O. Kherif, S. Chiheb, M. Teguar, A. Mekhaldi, and N. Harid, "Time-domain modeling of grounding systems' impulse response incorporating nonlinear and frequency-dependent aspects," *IEEE Transactions on Electromagnetic Compatibility,* vol. 60, no. 4, pp. 907-916, 2017.
[23] N. A. Sabiha, M. Alsharef, I. B. Taha, E. E. Elattar, M. K. Metwaly, and A. M. Abd-Elhady, "Assessment of grounding grid for enhancing wind turbine service sustainability," *Ain Shams Engineering Journal,* vol. 12, no. 1, pp. 577-589, 2021.

Appendix A: Calculation of double-exponential parameters

For transparency and reproducibility, the computation of the double-exponential model parameters used in Eq. (12) is presented here. The assumed lightning parameters (as in ref. [22]) are:

$$T_1 = 3.4\ \mu s, T_2 = 13.5\ \mu s, I_p = 28.51553\ kA$$

The relations used (Eqs. 11.1–11.3) are:

$$\alpha = \frac{0.69}{T_2}$$

$$\beta = \frac{2.2}{T_1}$$

$$I_0 = \frac{I_p}{1 + (\frac{\beta}{\alpha})(\ln\frac{\alpha}{\beta} - 1)}$$

Substituting numbers gives:

$$\alpha = \frac{0.69}{13.5 \times 10^{-6}} \approx 5111.11\ s^{-1}$$

$$\beta = \frac{2.2}{3.4 \times 10^{-6}} \approx 594594.6\ s^{-1}$$

Using the formula for I_0 yields $I_0 \approx 30\ kA$. These numeric values were applied in the CDEGS simulations (see Section 3.1).